

## Accepted Manuscript

Mechanisms of deformation-induced trace element migration in zircon resolved by atom probe and correlative microscopy

Steven M. Reddy, Arie van Riessen, David W. Saxey, Tim E. Johnson, William D.A. Rickard, Denis Fougereuse, Sebastian Fischer, Ty J. Prosa, Katherine P. Rice, David A Reinhard, Yimeng Chen, David Olson

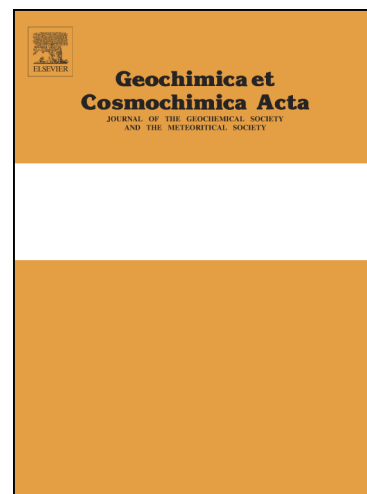
PII: S0016-7037(16)30534-8  
DOI: <http://dx.doi.org/10.1016/j.gca.2016.09.019>  
Reference: GCA 9931

To appear in: *Geochimica et Cosmochimica Acta*

Received Date: 10 May 2016  
Accepted Date: 15 September 2016

Please cite this article as: Reddy, S.M., Riessen, A.v., Saxey, D.W., Johnson, T.E., Rickard, W.D.A., Fougereuse, D., Fischer, S., Prosa, T.J., Rice, K.P., Reinhard, D.A., Chen, Y., Olson, D., Mechanisms of deformation-induced trace element migration in zircon resolved by atom probe and correlative microscopy, *Geochimica et Cosmochimica Acta* (2016), doi: <http://dx.doi.org/10.1016/j.gca.2016.09.019>

This is a PDF file of an unedited manuscript that has been accepted for publication. As a service to our customers we are providing this early version of the manuscript. The manuscript will undergo copyediting, typesetting, and review of the resulting proof before it is published in its final form. Please note that during the production process errors may be discovered which could affect the content, and all legal disclaimers that apply to the journal pertain.



1

2 Mechanisms of deformation-induced trace element migration in  
3 zircon resolved by atom probe and correlative microscopy

4

5

6 **Steven M. Reddy<sup>a,b,\*</sup>, Arie van Riessen<sup>a,c</sup>, David W. Saxey<sup>a,c</sup>, Tim E. Johnson<sup>b</sup>,**  
7 **William D. A. Rickard<sup>a,c</sup>, Denis Fougere<sup>a,b</sup>, Sebastian Fischer<sup>d</sup>, Ty J. Prosa<sup>e</sup>,**  
8 **Katherine P. Rice<sup>e</sup>, David A Reinhard<sup>e</sup>, Yimeng Chen<sup>e</sup>, David Olson<sup>e</sup>**

9

10 <sup>a</sup> *Geoscience Atom Probe, Advanced Resource Characterisation Facility, John de Laeter*  
11 *Centre, Curtin University, GPO Box U1987, Perth, WA 6845, Australia*

12 <sup>b</sup> *Department of Applied Geology, The Institute for Geoscience Research (TIGeR), Western*  
13 *Australian School of Mines, Curtin University, GPO Box U1987, Perth, WA 6845, Australia.*

14 <sup>c</sup> *Department of Physics and Astronomy, Curtin University, GPO Box U1987, Perth, WA*  
15 *6845, Australia.*

16 <sup>d</sup> *Department of Earth and Environmental Sciences, University of St Andrews, St Andrews,*  
17 *Fife, KY16 9AL, UK.*

18 <sup>e</sup> *CAMECA Instruments Inc., 5500 Nobel Drive, Madison, WI 53711, USA.*

19 \* Corresponding author: s.reddy@curtin.edu.au

20

21 **Keywords:**

22 atom probe microscopy, nanoscale, zircon, trace element, geochemistry, microstructure,  
23 EBSD, reidite, impact

24 **Abstract**

25

26 The widespread use of zircon in geochemical and geochronological studies of crustal  
27 rocks is underpinned by an understanding of the processes that may modify its  
28 composition. Deformation during tectonic and impact related strain is known to modify  
29 zircon trace element compositions, but the mechanisms by which this occurs remain  
30 unresolved. Here we combine electron backscatter diffraction, transmission Kikuchi  
31 diffraction and atom probe microscopy to investigate trace element migration  
32 associated with a ~20 nm wide, 2° low-angle subgrain boundary formed in zircon  
33 during a single, high-strain rate, deformation associated with a bolide impact. The low-  
34 angle boundary shows elevated concentrations of both substitutional (Y) and interstitial  
35 (Al, Mg & Be) ions. The observed compositional variations reflect a dynamic process  
36 associated with the recovery of shock-induced vacancies and dislocations into lower  
37 energy low-angle boundaries. Y segregation is linked to the migration and localization of  
38 oxygen vacancies, whilst the interstitial ions migrate in association with dislocations.  
39 These data represent the direct nanoscale observation of geologically-instantaneous,  
40 trace element migration associated with crystal plasticity of zircon and provide a  
41 framework for further understanding mass transfer processes in zircon.

42 **1. Introduction**

43

44 Zircon ( $\text{ZrSiO}_4$ ) is a common accessory mineral that occurs in most crustal rocks. The  
45 low diffusivity of most trace elements through the zircon lattice, inferred from trace  
46 element zonation (Vavra, 1990; Hoskin, 2000) and diffusion experiments (Cherniak et  
47 al., 1997; Cherniak and Watson, 2003; Cherniak and Watson, 2007), make zircon a  
48 robust geochemical repository. Hence, the trace and rare earth elements (REE)  
49 incorporated into the zircon are commonly used to place valuable constraints on  
50 petrogenetic processes (Hoskin and Schaltegger, 2003). For example, the trace element  
51 geochemistry of zircon yields source rock type and crystallization conditions of igneous  
52 rocks (Belousova et al., 2002; Ferry and Watson, 2007; Hanchar and van Westrenen,  
53 2007; Grimes et al., 2009; Claiborne et al., 2010) and can place constraints on  
54 recrystallization mechanisms, hydrothermal alteration and the histories of metamorphic  
55 rocks (Hoskin and Black, 2000; Hoskin, 2005; Harley et al., 2007; Marsh and Stockli,  
56 2015). The trace element composition of zircon also has economic importance, for  
57 example being used to assess the prospectivity of granites for mineralisation (Ballard et  
58 al., 2002; Dilles et al., 2015).

59

60 The incorporation of trace amounts of uranium, and its subsequent radioactive decay to  
61 lead, enables the U-Pb dating of zircon to place temporal constraints of numerous  
62 crustal processes (Harley and Kelly, 2007; Corfu, 2013). When combined with Lu-Hf and  
63 oxygen isotopic data, zircon can be used to constrain crustal evolution over a range of  
64 timescales (Hawkesworth and Kemp, 2006; Parman, 2015; Payne et al., 2016). In  
65 addition, the ability of zircon to withstand weathering, erosion, sedimentary transport  
66 and diagenesis, make zircon a common target for sedimentary provenance analysis

67 (Fedo et al., 2003; Gehrels, 2014) and the geochemistry and geochronology of ancient  
68 detrital zircon grains is the principal means of understanding petrogenetic processes  
69 and environmental conditions in the earliest stages of Earth history (Maas et al., 1992;  
70 Wilde et al., 2001; Hoskin, 2005; Watson and Harrison, 2005; Harrison and Schmitt,  
71 2007; Ushikubo et al., 2008; Harrison, 2009). Complementing the terrestrial studies of  
72 Hadean zircon are analyses from lunar and meteoritic zircon samples, that provide  
73 fundamental constraints on the early solar system and planetary evolution (Nemchin et  
74 al., 2010; Humayun et al., 2013; Izuka et al., 2015). However, despite this broad  
75 application of zircon in geochemical and geochronological studies, it is widely  
76 recognised that a number of different processes may modify the trace element  
77 compositions of zircon.

78  
79 Radiation damage within zircon can facilitate trace element redistribution and the  
80 incorporation of non-formula elements (Ewing et al., 2003; Palenik et al., 2003; Horie et  
81 al., 2006) even under low temperature hydrothermal conditions (Geisler et al., 2002;  
82 Pidgeon, 2014). Trace element modification associated with radiation damage reflects a  
83 complex interaction of the self-irradiation process, enhanced diffusion along radiation-  
84 induced defects, and reactions associated with fluid ingress by radiation-enhanced  
85 fractures and recrystallization (Geisler et al., 2007; Nasdala et al., 2010).

86  
87 Detailed microstructural characterization has demonstrated that crystal plastic  
88 deformation of zircon may take place in Earth's crust due to tectonic processes (Reddy  
89 et al., 2007; Reddy et al., 2009; Piazzolo et al., 2012) and meteorite impact events (Moser  
90 et al., 2011; Cavosie et al., 2015). Geochemical analyses of deformed zircon indicate that  
91 trace element compositions may be modified in the vicinity of intracrystalline defects,

92 particularly in the regions of low-angle boundaries (Reddy et al., 2006; Timms et al.,  
93 2006; Moser et al., 2009; Nemchin et al., 2009; Moser et al., 2011; Timms et al., 2011;  
94 Piazzolo et al., 2016). A number of models have been proposed to explain the observed  
95 relationship between microstructure and trace element migration including enhanced  
96 diffusion along dislocation pipes and low-angle boundaries (Reddy et al., 2006; Moser et  
97 al., 2011; Timms et al., 2011; Piazzolo et al., 2016), incorporation of trace elements within  
98 migrating dislocations (Reddy et al., 2006; Reddy et al., 2007; Piazzolo et al., 2016) and  
99 creep cavitation (Timms et al., 2012a). However, crystal defects may also trap trace  
100 elements; for example, Pb has been shown to segregate into dislocation loops during  
101 metamorphism (Peterman et al 2016).

102

103 Constraining the processes that are responsible for deformation-related compositional  
104 modification of zircon has remained elusive because the volume of material typically  
105 needed to characterize compositional heterogeneities (100s of  $\mu\text{m}^3$ ) is considerably  
106 larger than the sub-micron scale microstructures in which these heterogeneities occur.  
107 Direct comparison with compositional data has required averaging of quantitative  
108 microstructural data over similar volumes to those measured by quantitative analytical  
109 techniques (Timms et al., 2006; Timms et al., 2011). Higher spatial resolution analytical  
110 methods, for example hyperspectral cathodoluminescence (CL) data, indicate variations  
111 in the concentrations of trivalent REEs at the micrometre scale, but these are not  
112 quantitative (Reddy et al., 2006; Timms and Reddy, 2009; Timms et al., 2011). As a  
113 result, the spatial relationships between deformation microstructures and  
114 compositional variations, as well as the processes responsible for trace element mobility  
115 in deformed or defect-enriched zircon, have proved difficult to resolve.

116

117 The recent applications of atom probe microscopy to zircon have highlighted the  
118 potential for this analytical technique to quantify nanoscale compositional variations  
119 and establish the controls and processes associated with trace element modification  
120 (Valley et al., 2014; Valley et al., 2015; Peterman et al., 2016; Piazzolo et al., 2016). Here  
121 we combine electron backscatter diffraction (EBSD), transmission Kikuchi diffraction  
122 (TKD) and atom probe microscopy to investigate the nanoscale relationships between  
123 microstructure and trace element composition in a zircon grain that records a single  
124 shock deformation event associated with a meteorite impact.

## 125 **2. Sample and Analytical Procedures**

126

### 127 *2.1 Sample Description*

128

129 The Stac Fada Member of the Stoer Group of sedimentary rocks in NW Scotland  
130 represents an ejecta deposit associated with a meteorite impact ~1.18 billion years ago  
131 (Amor et al., 2008; Parnell et al., 2011; Reddy et al., 2015). The unit extends some 50 km  
132 along strike and has a variable thickness that in places exceeds 20 m (Fig. 1). It  
133 comprises three main facies types attributed to deposition from a single decelerating  
134 granular density current (Branney and Brown, 2011). The analysed sample (14-SF-01)  
135 was collected from the basal layer of the Stac Fada Member (UK Grid Reference NC  
136 03348 28515 equivalent to Latitude 58.2014, Longitude -5.3482 in WGS84) (Fig. 1) and  
137 is a matrix-supported, poorly-sorted breccia comprising centimetre size clasts of lithic  
138 and devitrified melt fragments. The sample shows no evidence of deformation or  
139 metamorphism at the hand specimen scale. This is consistent with previous reports that  
140 the Stac Fada Member underwent diagenesis immediately after deposition (Parnell et  
141 al., 2011) and has only undergone low-grade (prehnite-pumpellyite facies) regional  
142 metamorphism and negligible post-impact deformation (Simms, 2015).

143

144 *2.2 Methodologies*

145

146 Details of the zircon separation, concentration and mounting methodologies have been  
147 described in detail elsewhere (Reddy et al., 2015) and only a brief summary is provided  
148 here.

149

150 Approximately 2 kg of sample 14-SF-01 was disaggregated using SelFrag high-voltage  
151 pulse power fragmentation at the Department of Applied Geology, Curtin University.

152 Short pulses of high-voltage electrical fields were applied with a frequency of 2 Hz over  
153 a decreasing range of voltages and electrode gaps. As the sample was progressively

154 disaggregated, grains and fragments smaller than 410  $\mu\text{m}$  fell through an integrated  
155 mesh and into a collection vessel, which is isolated from further electrical pulses.

156 Previous studies indicate that SelFrag does not lead to significant increases in the  
157 temperature or pressure of the separated phases and has no noticeable effect on zircon  
158 grains (Giese et al., 2010).

159

160 The disaggregated sample was sieved using a 355  $\mu\text{m}$  disposable mesh and sodium  
161 polytungstate (NaPT) solution (specific gravity =2.85) was used to concentrate zircon  
162 grains in the <355  $\mu\text{m}$  fraction. A hand magnet was used to remove the magnetic  
163 fraction and the remaining grains were passed through a Franz magnetic separator with  
164 the magnetic fractions being drawn off in increments of 0.2 to 0.5 amps over a range of  
165 current settings from 0.1 to 1.7A. The non-magnetic (>1.7A) fraction was then hand-  
166 picked for zircon. Approximately 200 separated zircon grains were investigated (Reddy  
167 et al., 2015) but data from only one of these (grain 86) are reported here.

168



169 EBSD and CL imaging of grain 86 was conducted on a Tescan MIRA3 Field Emission SEM  
170 with Oxford Instruments AZtec EBSD system, housed in the Microscopy & Microanalysis  
171 Facility (John de Laeter Centre) at Curtin University. CL imaging was undertaken using a  
172 Tescan panchromatic CL detector with 185-850 nm spectral range at 10 kV accelerating  
173 voltage and a working distance of 16mm. EBSD data were acquired using the automatic  
174 mapping capability of Oxford Instruments AZtec 2.3 software. Match units used for  
175 indexing were derived from published crystallographic data for zircon (Hazen and  
176 Finger, 1979) and reidite (Farnan et al., 2003). For grain 86, a 200 nm grid was used to  
177 systematically collect ~530,000 electron backscatter patterns. The EBSD data were  
178 post-processed using Oxford Instruments Channel 5.12 software to remove 'wildspikes'  
179 and interpolate non-indexed points using a 6 or 7 nearest neighbor filter following  
180 standard procedures for zircon EBSD analysis (Reddy et al., 2007). The post-processed  
181 data files were then used to generate EBSD maps.

182

183 Atom probe microscopy is a technique that allows the sub-nanometre scale, 3D imaging  
184 of atoms across the whole periodic table (Kelly and Larson, 2012; Larson et al., 2013b).  
185 The technique involves time-controlled field evaporation of atoms by applying a high-  
186 voltage electric field to a needle-shaped sample whose tip is then heated by a pulsing UV  
187 laser. Ideally, the instrument is set up such that a single atom is field evaporated every  
188 ~100 laser pulses. On evaporation, the atom is immediately ionized and accelerated by  
189 the field toward a position-sensitive detector. The x-y coordinates of the detector  
190 impact, combined with the order in which the ions hit the detector, allows  
191 reconstruction of the original position of the atoms in the sample (Gault et al., 2009;  
192 Larson et al., 2013a). The time-of-flight between the laser pulse and the detector impact  
193 is a function of the mass-to-charge ratio ( $m/z$ ) of the emitted ion, and is used to identify

194 the atom species emitted from the tip. The charge of the emitted ion does not represent  
195 the original charge of the species in the analysed sample, but is induced by the electric  
196 field immediately after evaporation (Kingham, 1982). This charge is therefore largely a  
197 function of experimental run conditions and sample morphology (Larson et al., 2013b).

198

199 The mass spectrometry data is reported in the form of a histogram (mass spectrum), in  
200 which the number of counts is plotted against intervals in  $m/z$ . Peaks in the mass  
201 spectrum that sit above the background noise level are identified and delineated  
202 manually, a process referred to as 'ranging'. The ions that form the ranged peaks are  
203 then used, with their  $x$ ,  $y$  and  $z$  positions, to reconstruct the chemical identities and  
204 original 3D locations of the analysed atoms. Typical data sets comprise millions to tens  
205 of millions of atoms.

206

207 In contrast to most zircon analytical approaches, atom probe microscopy does not use a  
208 standard in the same manner as in ion- and electron-probe techniques. The APM  
209 technique does not lend itself to correction using standards as the analysis conditions  
210 cannot be reliably replicated between the standard and the specimen of interest. In  
211 general, the voltage applied to the specimen, the heating from the laser pulse and the  
212 shape of the specimen tip cannot be held constant between two acquisitions, and it is  
213 not clear that a discrepancy in the result from the standard analysis can be carried over  
214 and applied directly to the data of interest. However, past experience with other  
215 materials, and more recent APM studies of zircon (Valley et al., 2014; Valley et al., 2015;  
216 Peterman et al., 2016; Piazzolo et al., 2016) provide a basis for confidence in the  
217 measured concentrations of trace elements reported here.

218

219 Atom probe specimens were prepared by focussed ion beam milling at CAMECA  
220 Instruments Inc., Madison, Wisconsin, USA. A region of interest, identified from the  
221 EBSD data, was targeted for site-specific atom probe sample preparation. A FEI Helios  
222 Nanolab 660 dual beam FIB-SEM was used to fabricate atom probe specimens on a  
223 microtip coupon (Thompson et al., 2007b). Tip sharpening was undertaken using  
224 several annular milling steps, each with progressively smaller inner radii and reduced  
225 beam currents. A final cleaning at 5kV was undertaken to remove most of the ion-milling  
226 induced gallium and surface contamination.

227

228 During the sharpening process, TKD analysis of the atom probe needles was carried out  
229 on a FEI Nova NanoLab 600 dual beam FIB-SEM equipped with an EBSD system from  
230 EDAX. TKD is capable of providing high spatial resolution orientation mapping for atom  
231 probe specimens (Babinsky et al., 2014) and was conducted with a 20 kV electron beam  
232 with a step size of ~10 nm. TKD data acquired using the EDAX system were exported as  
233 .ang files and post-processed using Oxford Instruments Channel 5.12 software.

234

235 Atom probe results were acquired using the CAMECA LEAP 5000 XR in laser pulsing  
236 mode with initial and final voltages of 3.2 kV and 4.6 kV respectively. Data acquisition  
237 utilised a 355 nm laser with pulse energy of ~250 pJ, focussed to a spot-size less than  
238 0.5  $\mu\text{m}$  at the specimen apex, and operating at a frequency ~180 kHz. The specimens  
239 were kept at a temperature of 30 K to inhibit thermally induced ion migration on the tip  
240 surface during field ionisation, and the ion detection rate was set to 0.01 ions per pulse  
241 (Larson et al., 2013b).

242

243 Atom probe data were acquired using LAS Root version 15.41.351, reconstructed with  
244 CAMECAROOT version 15.43.393e, and analysed with version 3.6.10 of Cameca's  
245 Interactive Visualisation and Analysis Software (IVAS).  $m/z$  values from 0-300 Da were  
246 recorded, and the background throughout the experiment was around 20 ppm/nsec, as  
247 reported by CAMECAROOT. The mass resolving power for the time-of-flight spectrum  
248 ( $M/\Delta M$ ) was measured at  $\sim 1150$  for the  $^{16}\text{O}_2^+$  peak. For peak ranging, mass peaks were  
249 compared to the local background and only those regions above twice the background  
250 level were ranged. The reconstruction stage used an initial tip radius of 25nm, and a  
251 constant shank angle of  $5^\circ$ . Features observed by SE imaging and TKD were adopted to  
252 validate the parameters used in 3D reconstruction.

253

254 Trace element chemical analysis was performed using a combination of iso-  
255 concentration surfaces (iso-surfaces) and proximity histograms (proxigrams). An iso-  
256 surface is a 2-dimensional contour of constant chemical concentration, with regions  
257 above a threshold level of concentration on one side of the boundary and lower  
258 concentrations on the other. Proxigrams are 1-dimensional concentration profiles that  
259 are plotted against the perpendicular distance from a particular iso-surface. Iso-surfaces  
260 are generally curved, and the proxigram analysis conducted by IVAS uses a sophisticated  
261 algorithm to calculate distances from the reference surface (Hellman et al., 2000).

262

### 263 **3. Results**

264 Cathodoluminescence imaging of grain 86 shows a complicated microstructure  
265 comprising a dark CL-poor core surrounded by intermediate region and a bright CL rim  
266 (Fig. 2a). A band contrast map of the zircon grain, which reflects the quality of EBSD

267 patterns in different parts of the grain, shows additional complexity in the dark CL core.  
268 A series of  $\sim 2\ \mu\text{m}$  wide, parallel lamellae, seen in both CL and band contrast maps, cut  
269 across the brighter CL zones, but do not penetrate into the dark CL core. These bands  
270 are shown by the EBSD data to be reidite, the high-pressure  $\text{ZrSiO}_4$  polymorph (Fig. 2c).  
271 This reidite, the focus of a previous study (Reddy et al., 2015), along with the host  
272 zircon, record variations in lattice orientation expressed by the presence of discrete low-  
273 angle orientation boundaries that each accommodate  $0.5\text{--}2^\circ$  of misorientation and  
274 together accommodate a total of  $\sim 16^\circ$  lattice variation across the whole grain (Fig. 2c).  
275 The distribution of low-angle boundaries in the zircon is complicated but broadly  
276 follows the spatial distribution of the reidite (Fig. 2c,d). One of these low-angle  
277 boundaries is captured in the atom probe specimen (Fig. 3). This boundary coincides  
278 with a  $\sim 2^\circ$  change in orientation recorded by the TKD data (blue-green contact in Fig. 3).  
279 In addition, the TKD data indicate that the atom probe specimen comprises only zircon,  
280 with no evidence for reidite along the identified orientation boundary (Fig. 3).  
281  
282 Atom probe analysis of the zircon specimen shows a complex mass spectrum, which  
283 reflects the evaporation of single ions and molecular species at the +1 to +4 charge  
284 states (Fig. 4). Most peaks represent the major elements found in zircon with only a few  
285 trace element peaks being detected. The chemical sensitivity of the atom probe is often  
286 around 10 ppma, but the exact detection limit depends on the location and number of  
287 the expected peaks. Many of the REEs are likely to appear in the mass spectrum as  
288 doubly or triply charged ions, as well as possibly doubly and triply charged oxides. This  
289 means that REE peaks may be divided between a large number of mass peaks within the  
290 spectrum, significantly diluting the signal strength at any specific  $m/z$  value. Minimizing

291 this dilution effect, by optimizing atom probe acquisition parameters for specific trace  
292 elements, is an area of future research.

293

294 Reconstruction of the data reveals a ~20 nm wide zone of trace element enrichment  
295 associated with the orientation boundary (Fig. 5). The zone shows increased  
296 concentrations in Y (0.735 at.%), Al (0.543 at.%), Be (0.055 at.%) and Mg (0.029 at.%)  
297 associated with a decrease in Zr (Table 1). These trace element concentrations  
298 represent significant increases from those measured in the host zircon (Fig. 5).

299 Proximity histograms for the upper and lower boundaries of the enriched zone show  
300 that trace element concentrations are not constant across the low-angle boundary, with  
301 Y showing narrow maxima ~3 nm just inside both of the two boundary interfaces, and  
302 Al, Be and Mg exhibiting broader maxima around 4–5 nm inside the interfaces (Fig. 6).  
303 The concentration of Mg also shows a slight maximum outside the lower interface; a  
304 feature that is missing from the upper interface (Fig 5, 6).

305

306 Rare earth element, actinide and Pb distributions within the sample are below the  
307 detection sensitivity (50-100 appm, 50 appm, and 50 appm respectively) - as  
308 determined by the background noise local to these positions within the mass spectrum  
309 (Figure 4). Similarly, there is no observable phosphorus peak (~100 appm detection  
310 sensitivity) in the atom probe mass spectrum. This absence of P limits the extent of  
311 xenotime (YPO<sub>4</sub>) substitution in the zircon lattice. The detection limits are relatively  
312 high due to the tails on the mass peaks between 14 and ~100 Da. These elevate the local  
313 background noise by up to 10 times its intrinsic value, and make the detection of trace  
314 elements in this part of the spectrum more difficult. Several factors may influence the  
315 shape of the mass peaks and their tails (Larson et al., 2013b), but the most likely cause

316 in this case is poor thermal conductivity in the atom probe specimen, leading to an  
317 extended period of ion evaporation while the tip is cooling after the laser pulse.

318

## 319 **4. Discussion**

### 320 **4.1 Zircon Microstructure**

321

322 Cathodoluminescence data from a zircon grain from the Stac Fada impactite shows the  
323 presence of three CL-distinct zones (Fig. 2a); a dark CL core, a bright CL rim and an  
324 intermediate zone between them. Such CL variations in zircon are normally attributed to  
325 compositional zoning of trace elements associated with growth (Corfu et al., 2003). In  
326 this case, the zones identified in CL are interpreted to represent a complex igneous and  
327 metamorphic evolution prior to the reidite-forming impact event. Based on provenance  
328 analysis of the Stac Fada zircon population (Rainbird et al., 2001), this evolution is  
329 interpreted to reflect the complex tectonic and metamorphic history of the Lewisian  
330 target rocks.

331

332 Reidite is the high pressure polymorph of  $ZrSiO_4$  (Glass et al., 2002) and its presence in  
333 the rims of grain 86 demonstrates that the zircon underwent shock deformation of >30  
334 GPa associated with an impact event at ~1.18 Ga (Reddy et al., 2015). Reidite in the  
335 grain is limited to the outermost two compositional zones and stops abruptly at the CL  
336 dark core. The low CL emission from the core is consistent with radiation-damage  
337 associated with the presence of U and Th. Hence, the absence of reidite from the core of  
338 the zircon indicates that the formation of reidite is intimately linked to the crystallinity  
339 of the host zircon and that partial metamictization is likely to inhibit the development of  
340 reidite in shock environments. This is consistent with previous observations (Wittmann  
341 et al., 2006). Furthermore, the observation that low-angle boundaries are preferentially

342 located within the areas of reidite development may indicate that radiation damage of  
343 zircon inhibits the formation and/or migration of dislocations.

344

345 A bolide impact event would produce an immense number of defects (vacancies and  
346 dislocations) within the shocked grain. However, the microstructure of both zircon and  
347 reidite is characterized by the presence of discrete low-angle boundaries that each  
348 accommodate  $<2^\circ$  lattice distortion (Fig. 2c,d). The presence of low-angle boundaries in  
349 deformed zircon has previously been interpreted to represent the migration of  
350 dislocations into lower energy configurations. Such an interpretation is based on the  
351 geometry of the boundary with respect to the crystal lattice (Reddy et al., 2007). The  
352 low-angle boundary captured within the atom probe sample, and imaged by TKD  
353 analysis, shows no evidence of reidite and accommodates  $\sim 2^\circ$  of misorientation.  
354 However, analysis of orientation differences and the low-angle boundary geometry (not  
355 presented) are not associated with any previously reported rational zircon slip system  
356 (summarized by Timms et al., 2012b). Previous estimates of the dislocation density of  
357  $10^{14} \text{ m}^{-2}$  in  $2^\circ$  low-angle boundaries associated with tectonic-induced  $\langle 001 \rangle \{100\}$  slip  
358 (Reddy et al., 2007) are similar to those derived from studies of unrecovered, reidite-  
359 bearing, experimentally shock-deformed zircon (Leroux et al., 1999). Thus, we interpret  
360 the low-angle boundary in the atom probe specimen to have formed by the migration  
361 and complex interaction of a large number of multiple defect types (vacancies and  
362 dislocations) that formed almost instantaneously by shock-deformation of zircon.

363

364 The recovery of minerals by the migration of defects into boundaries may take place in  
365 thermal or deformation events that significantly postdate the deformation event that  
366 caused them. However, the absence of any significant thermal or deformation events



367 following the deposition of the Stac Fada Member precludes this. The observation that  
368 the formation of the low-angle boundaries post-dates the formation of reidite (Reddy et  
369 al., 2015), places further temporal constraints on recovery, and indicates that the  
370 observed recovery must be related to the latter stages of the impact process. This is  
371 consistent with predictions of the evolution of impact-related zircon microstructure  
372 based on shock deformation mechanism maps for  $ZrSiO_4$  (Timms et al., 2012b). Thus,  
373 low-angle boundaries within the zircon are interpreted to reflect immediate post-impact  
374 recovery of defects formed during bolide impact.

375

#### 376 **4.2. Trace Element Compositions in the Zircon Host**

377 In undeformed zircon the substitution of trivalent REEs and  $Y^{3+}$  for  $Zr^{4+}$  requires  
378 additional trace element substitutions to maintain charge balance and several different  
379 mechanisms have been postulated (Cherniak, 2010). In this study, P is below  
380 background noise levels, the ratio of Y to P is therefore high, and there is a spatial  
381 correlation between Y and the interstitial elements Al, Mg and Be both in the host zircon  
382 and the low-angle boundary. These three interstitial elements are not commonly  
383 analysed in zircon. However, when such analyses are undertaken then these elements  
384 have been reported to be incorporated into zircon at trace levels during growth (Speer,  
385 1980; Hinton and Upton, 1991; Hoskin et al., 2000; Wiedenbeck et al., 2004). Charge  
386 compensation substitutions based on the ratio of (REE, Y) to P indicate that the  
387 important substitutions within the pre-shocked zircon were probably  $(Mg, Be)^{2+}_{(int)} +$   
388  $3Y^{3+} + P^{5+} = 3Zr^{4+} + Si$  and  $Al^{3+}_{(int)} + 4Y^{3+} + P^{5+} = 4Zr^{4+} + Si$  (Hoskin et al., 2000). Since P in  
389 zircon tends to increase with magmatic differentiation, the high, pre-shock, Y/P ratio  
390 ( $>3$ ) of the zircon points to derivation from a mafic source (Hoskin et al., 2000). The  
391 presence of hydrated mafic and ultramafic rocks in the impact target zone (Johnson et

392 al., 2012) may explain the presence of spherules of basaltic composition within the Stac  
393 Fada Member, a feature that some find difficult to reconcile with a non-volcanic origin  
394 for the unit (Goodenough and Krabbendam, 2011).

395

#### 396 **4.3 Trace Element Variations and Microstructure**

397 A model to explain the variations in Y, Al, Mg and Be within the atom probe specimen  
398 must account for the spatial coincidence of trace element enrichment and low-angle  
399 boundary formation (Figs. 3, 5), and the similar behaviour of both substitutional Y and  
400 interstitial Al, Mg and Be ions. The close spatial and temporal relationship between  
401 trace element segregation and the low-angle boundary indicates that the two features  
402 developed concurrently and are intimately linked. Such an interpretation is consistent  
403 with the general observation that increasing lattice misorientations, and therefore  
404 increasing dislocation density, are associated with increasing trace element segregation  
405 in metals and alloys (Watanabe, 1985).

406

407 The short-range segregation of solute atoms at interfaces is well established in the  
408 materials science literature and is recognized as a complex process that is controlled by  
409 a range of extrinsic (pressure, temperature) and intrinsic (elastic and electrostatic  
410 interactions between solute and host atoms) variables (Sutton and Balluffi, 2006).

411 Although there is very little detailed analysis of such processes in minerals, it is clear  
412 that the segregation of trace elements into the low-angle boundary must be  
413 energetically favourable compared to maintaining the trace elements in the host zircon.  
414 However, the mechanisms responsible for segregation remain enigmatic and a number  
415 of factors may contribute to the driving force for trace element migration.

416

417 Principal amongst the drivers for substitutional ion migration is elastic strain energy  
418 associated with differences in ionic sizes between the trace element and host. Molecular  
419 dynamic and *ab-initio* modelling of point defect formation in zircon indicate that the  
420 production and migration of oxygen vacancies is likely to be energetically favourable  
421 over other defect sites (Meis and Gale, 1998; Crocombette and Ghaleb, 2001; Park et al.,  
422 2001) and the exchange of  $Y^{3+}$  on the  $Zr^{4+}$  site is likely to be intimately linked to oxygen  
423 vacancies for charge compensation (Akhtar and Waseem, 2001). The close relationship  
424 between oxygen vacancies and trace element migration may provide an explanation for  
425 the observed Y increase within the zircon low-angle boundary with initial segregation of  
426 Y due to elastic interactions being charge balanced by subsequent vacancy migration  
427 (Sun et al., 2015). However, although such a model explains the observed Y enrichment  
428 in the low-angle boundary, it fails to account for the heterogeneous distribution of Y  
429 close to the interfaces of the low-angle boundary (Fig. 6).

430

431 Hybrid Monte Carlo – molecular dynamic simulations of Y-stabilised zirconia ( $ZrO_2$ )  
432 predict the migration of oxygen vacancies into lattice orientation boundaries, due to  
433 lower vacancy energies at these microstructural locations, rather than being driven by  
434 elastic strain associated with ion size differences (Lee et al., 2013). In  $ZrO_2$ , it is  
435 energetically favourable for these oxygen vacancies to be associated with yttrium ions  
436 (Yoshiya and Oyama, 2011; Lee et al., 2013) and segregation reduces lattice strains in  
437 the boundary (Yoshiya and Oyama, 2011). Although such models cannot be  
438 quantitatively applied to  $ZrSiO_4$ , the qualitative distribution of  $Y^{3+}$  for  $Zr^{4+}$  associated  
439 with lattice orientation boundaries in  $ZrO_2$  (Lee et al., 2013) are similar to the peaks of Y  
440 distribution recorded by the atom probe data for  $ZrSiO_4$  in this study (Fig. 6). Based on

441 the atom probe data presented here, this model seems to be a more likely mechanism  
442 than diffusion of Y driven solely by elastic strain.

443

444 In addition to substitutional Y ions, the low-angle boundary is also enriched in the  
445 interstitial trace elements Al, Mg and Be. The relationship between interstitial trace  
446 elements and dislocations is well known. Modelling of the elastic field around a  
447 dislocation predicts that interstitial atoms will concentrate around stationary  
448 dislocations (Cottrell and Bilby, 1949); a feature referred to as a “Cottrell atmosphere”.

449 Migrating dislocations may capture interstitial elements and continue to move.

450 However, increasing concentrations of interstitial elements around an individual  
451 dislocation may halt its migration. Hence, the interstitial nature of Al, Mg and Be ions in  
452 the low-angle boundary is consistent with a two-stage process of interstitial migration  
453 into Cottrell atmospheres around shock-induced dislocations and the subsequent  
454 migration of both the dislocations and interstitial Cottrell atmospheres into low-angle  
455 boundaries during post-impact recovery. The additional complication of the asymmetric  
456 distribution of Mg immediately outside the lower interface of our sample may reflect  
457 asymmetric energy distributions outside the dislocation plane as modelled by kinetic  
458 Monte Carlo simulations of dislocation planes in silicon (Portavoce and Tréglia, 2014).

459

460 In contrast to non-geological materials where Cottrell atmospheres have been imaged  
461 (Blavette et al., 1999; Thompson et al., 2007a), there has been very little evidence for  
462 formation of Cottrell atmospheres in deforming minerals. Ando et al (2001) suggested a  
463 Cottrell atmosphere model for Fe–Mg variations associated with low-angle boundaries  
464 in olivine. A similar model has been inferred to explain Y mobility in tectonically  
465 deformed zircon (Piazolo et al., 2016). However, since Fe–Mg and Y–Zr exchange in

466 these minerals is substitutional in nature, these observations cannot be explained by a  
467 Cottrell atmosphere model. A similar point has been made (Portavoce and Tréglia, 2014)  
468 regarding interpretations of Cottrell atmospheres from atom probe studies of  
469 semiconductors (Thompson et al., 2007a; Duguay et al., 2010). In contrast, the data  
470 presented here provides compelling evidence for formation of Cottrell atmospheres  
471 associated with interstitial trace elements in zircon.

472

#### 473 **4.4 A model for trace element mobility in shocked zircon**

474 We interpret the enrichment of trace elements in the low-angle boundary to represent a  
475 combination of a) the migration of shock-induced oxygen vacancies into low-energy  
476 configurations at the low-angle boundary interface, coupled with segregation of Y into  
477 low energy sites, and b) interstitial migration of Al, Mg and Be as Cottrell atmospheres  
478 associated with dislocations that are migrating into low-angle boundary walls. The  
479 result is a charge compensated region of lattice distortion comprising both the enhanced  
480 substitutional and interstitial trace elements, as measured by the atom probe.

481

482 The nanoscale data presented here provide constraints on the processes by which trace  
483 element migration may occur in shock-deformed zircon. The data point to the important  
484 role of defect mobility, both vacancies and dislocations, in controlling the respective  
485 migration of both substitutional and interstitial ions. The high-strain rate nature of the  
486 impact, plus the extremely limited time for subsequent thermal modification of the  
487 zircon microstructure, indicate that the measured element migration is an extremely  
488 rapid and dynamic process, likely to be operating at the scale of seconds, linked to defect  
489 formation and mobility.

490

491 Similar relationships between microstructures and trace elements have been reported  
492 for tectonically-deformed zircon (Reddy et al., 2006; Timms et al., 2006; Timms and  
493 Reddy, 2009; Timms et al., 2011). These examples showed that defect mobility may also  
494 be the driver of the compositional modification of zircon during tectonic deformation.  
495 The observed relationships between low-angle boundary and trace element enrichment  
496 in zircon has often been considered to reflect fast diffusion of ions along the damaged  
497 core of a low-angle boundary (Reddy et al., 2006). However, such a long-range model  
498 does not explain variations in trace element compositions within the boundary zone and  
499 is not consistent with the short timescale available for the impact event. Although, fast  
500 diffusion along the low-angle boundary cannot be ruled out (Piazolo et al., 2016), the  
501 observations from the Stac Fada zircon are consistent with short-range mechanisms of  
502 low-angle boundary enrichment.

503

## 504 **5. Conclusions**

505 This research presents detailed quantitative microstructural analysis and compositional  
506 information at the nanoscale to yield unique insights into the relationships between  
507 deformation and the migration of chemical species in zircon during a single, high strain-  
508 rate, impact event. The data show that there is a clear spatial relationship between trace  
509 element compositions and low-angle boundaries formed by the recovery of defects in  
510 the later stages of the impact process. Migration of substitutional ions (Y) is associated  
511 with the migration of impact-induced oxygen vacancies to the lower energy sites  
512 associated with low-angle boundaries rather than elastic strain energies in the lattice.  
513 Interstitial ions (Al, Mg, Be) are inferred to migrate by the formation and migration of  
514 Cottrell atmospheres around impact-induced dislocations. The analysis of nanoscale  
515 compositional variations in zircon by atom probe microscopy provides a framework for

516 understanding the processes controlling the migration and modification of trace  
517 element compositions in deforming zircon.

518

### 519 **Acknowledgments**

520 The Australian Resource Characterisation Facility (ARCF) comprises state-of-the-art  
521 equipment to address fundamental science questions related to the resource sector. The  
522 facility is being developed under the auspices of the National Resource Sciences Precinct  
523 (NRSP) – a collaboration between CSIRO, Curtin University and The University of  
524 Western Australia – and is supported by the Science and Industry Endowment Fund  
525 (SIEF RI13-01). The authors gratefully acknowledge support of Curtin University's  
526 Microscopy & Microanalysis Facility and the John de Laeter Centre, whose  
527 instrumentation has been supported by University, State and Commonwealth  
528 Government funding. SMR acknowledges support from the ARC Core to Crust Fluid  
529 System COE (CE11E0070). We thank two anonymous reviewers and editor, Christian  
530 Koeberl, for constructive comments on the manuscript.

531

532 **Figure Captions**

533

534 Figure 1. Geological map showing the location of the Stac Fada Member and the sample  
535 site. Grid coordinates refer to the Ordnance Survey National Grid coordinate system.

536

537 Figure 2. Microstructural maps of the analysed zircon grain. a & b are after Reddy et al.,  
538 (2015). a) Panchromatic CL image showing dark CL core surrounded by an intermediate  
539 region and a bright CL rim. Planar black features in the CL emitting zircon are reidite  
540 lamellae. Less systematic black lines correspond to healed fractures shown in b. b) Band  
541 contrast (pattern quality) EBSD map. Brighter greyscale indicates higher pattern quality.  
542 c) EBSD texture component map of zircon (in red) overlain on the band contrast map  
543 shown in b. Lattice orientation variations are shown up to  $8^\circ$  from the white cross and  
544 total misorientation across the grain is  $16^\circ$ . Yellow lines show the locations of low-angle  
545 boundaries ( $0.6^\circ$ - $2.0^\circ$ ) within the zircon. Tourquoise lamellae represent reidite. The  
546 white square shows the location of map d. d) Close up of area in c. The white circle  
547 corresponds to the position of the analysed atom probe specimen.

548

549 Figure 3. a) Orientation map of the studied atom probe needle constructed from  
550 transmission Kikuchi diffraction data. The change from blue to green corresponds to a  
551 small-angle lattice misorientation accommodated by a  $2^\circ$  low-angle boundary. White  
552 box shows the area analysed by the atom probe following further focussed ion beam  
553 milling of the sample. Area below the green area, which has not indexed, reflects low  
554 pattern quality due to poor electron transmission through the thicker part of the  
555 specimen.

556



557 Figure 4. Atom probe mass spectrum obtained from the region of interest shown in Fig.  
558 3. The major  $m/z$  peaks are identified, including trace elements that were only present  
559 at detectable levels within the boundary region.

560

561 Figure 5. Reconstruction of atom probe data showing trace element variations for Y, Al,  
562 Be and Mg. The coloured spheres represent the positions of the illustrated elements but  
563 are not drawn to scale. Grey points defining the shape of the atom probe data set  
564 represent the positions of 10% of measured Zr atoms. The band showing increased  
565 concentration of trace elements corresponds to the position of the low-angle boundary  
566 in the region of interest in Fig. 3.

567

568 Figure 6. Proximity histograms showing composition variation in Y, Al, Be and Mg as a  
569 function of distance from the upper and lower boundary interfaces. The upper and  
570 lower interfaces are defined by concentration contours at 0.2% Y.

571

## 572 **Tables**

573 Table 1. Compositional data from host zircon matrix and low-angle boundary region  
574 derived from the atom probe data.

575

576

577

578 **References**

- 579 Akhtar, M. and Waseem, S. (2001) Atomistic simulation studies of zircon. *Chem. Phys.*  
580 **274**, 109-120.
- 581 Amor, K., Hesselbo, S.P., Porcelli, D., Thackrey, S. and Parnell, J. (2008) A precambrian  
582 proximal ejecta blanket from Scotland. *Geology* **36**, 303-306.
- 583 Babinsky, K., De Kloe, R., Clemens, H. and Primig, S. (2014) A novel approach for site-  
584 specific atom probe specimen preparation by focused ion beam and transmission  
585 electron backscatter diffraction. *Ultramicroscopy* **144**, 9-18.
- 586 Ballard, J.R., Palin, M.J. and Campbell, I.H. (2002) Relative oxidation states of magmas  
587 inferred from Ce(IV)/Ce(III) in zircon: application to porphyry copper deposits of  
588 northern Chile. *Contrib. Mineral. Petrol.* **144**, 347-364.
- 589 Belousova, E.A., Griffin, W.L., O'Reilly, S.Y. and Fisher, N.I. (2002) Igneous zircon: trace  
590 element composition as an indicator of source rock type. *Contrib. Mineral. Petrol.* **143**,  
591 602-622.
- 592 Blavette, D., Cadel, E., Fraczkiwicz, A. and Menand, A. (1999) Three-dimensional  
593 atomic-scale imaging of impurity segregation to line defects. *Science* **286**, 2317-2319.
- 594 Branney, M.J. and Brown, R.J. (2011) Impactoclastic density current emplacement of  
595 terrestrial meteorite-impact ejecta and the formation of dust pellets and accretionary  
596 lapilli: Evidence from stac fada, Scotland. *J. Geol.* **119**, 275-292.
- 597 Cavosie, A.J., Erickson, T.M., Timms, N.E., Reddy, S.M., Talavera, C., Montalvo, S.D., Pincus,  
598 M.R., Gibbon, R.J. and Moser, D. (2015) A terrestrial perspective on using *ex situ* shocked  
599 zircons to date lunar impacts. *Geology* **43**, 999-1002.

- 600 Cherniak, D. (2010) Diffusion in accessory minerals: zircon, titanite, apatite, monazite  
601 and xenotime. *Rev. Mineral. Geochem.* **72**, 827-869.
- 602 Cherniak, D. and Watson, E. (2007) Ti diffusion in zircon. *Chem. Geol.* **242**, 470-483.
- 603 Cherniak, D.J., Hanchar, J.M. and Watson, E.B. (1997) Rare-earth diffusion in zircon.  
604 *Chem. Geol.* **134**, 289-301.
- 605 Cherniak, D.J. and Watson, E.B. (2003) Diffusion in zircon. *Rev. Mineral. Geochem.* **53**,  
606 113-143.
- 607 Claiborne, L.L., Miller, C.F. and Wooden, J.L. (2010) Trace element composition of  
608 igneous zircon: a thermal and compositional record of the accumulation and evolution of  
609 a large silicic batholith, Spirit Mountain, Nevada. *Contrib. Mineral. Petrol.* **160**, 511-531.
- 610 Corfu, F. (2013) A century of U-Pb geochronology: The long quest towards concordance.  
611 *GSA Bulletin* **125**, 33-47.
- 612 Corfu, F., Hanchar, J.M., Hoskin, P.W.O. and Kinny, P. (2003) Atlas of Zircon Textures. *Rev.*  
613 *Mineral. Geochem.* **53**, 469-500.
- 614 Cottrell, A.H. and Bilby, B.A. (1949) Dislocation theory of yielding and strain ageing of  
615 iron. *Proc. Phys. Soc. A* **62**, 49-62.
- 616 Crocombette, J.-P. and Ghaleb, D. (2001) Molecular dynamics modeling of irradiation  
617 damage in pure and uranium-doped zircon. *J. Nucl. Mater.* **295**, 167-178.
- 618 Dilles, J.H., Kent, A.J.R., Wooden, J.L., Tosdal, R.M., Koleszar, A., Lee, R.G. and Farmer, L.P.  
619 (2015) Zircon compositional evidence for sulfur-degassing from ore-forming arc  
620 magmas. *Econ. Geol.* **110**, 241-251.

- 621 Duguay, S., Philippe, T., Cristiano, F. and Blavette, D. (2010) Direct imaging of boron  
622 segregation to extended defects in silicon. *App. Phys. Lett.* **97**, 242104.
- 623 Ewing, R.C., Meldrum, A., Wang, L., Weber, W.J. and Corrales, L.R. (2003) Radiation  
624 effects in zircon. *Rev. Mineral. Geochem.* **53**, 387-425.
- 625 Farnan, I., Balan, E., Pickard, C.J. and Mauri, F. (2003) The effect of radiation damage on  
626 local structure in the crystalline fraction of ZrSiO<sub>4</sub>: Investigating the <sup>29</sup>Si NMR response  
627 to pressure in zircon and reidite. *Am. Mineral.* **88**, 1663.
- 628 Fedo, C.M., Sircombe, K.N. and Rainbird, R.H. (2003) Detrital zircon analysis of the  
629 sedimentary record. *Rev. Mineral. Geochem.* **53**, 277-303.
- 630 Ferry, J.M. and Watson, E.B. (2007) New thermodynamic models and revised  
631 calibrations for the Ti-in-zircon and Zr-in-rutile thermometers. *Contrib. Mineral. Petrol.*  
632 **154**, 429-437.
- 633 Gault, B., Moody, M.P., de Geuser, F., Tsafnat, G., La Fontaine, A., Stephenson, L.T., Haley,  
634 D. and Ringer, S.P. (2009) Advances in the calibration of atom probe tomographic  
635 reconstruction. *J. App. Phys.* **105**, 034913.
- 636 Gehrels, G. (2014) Detrital Zircon U-Pb Geochronology Applied to Tectonics. *Ann. Rev.*  
637 *Earth Planet. Sci.* **42**, 127-149.
- 638 Geisler, T., Pidgeon, R.T., van Bronswijk, W. and Kurtz, R. (2002) Transport of uranium,  
639 thorium, and lead in metamict zircon under low-temperature hydrothermal conditions.  
640 *Chem. Geol.* **191**, 141-154.

- 641 Geisler, T., Schaltegger, U. and Tomaschek, F. (2007) Re-equilibration of zircon in  
642 aqueous fluids and melts. *Elements* **3**, 43-50.
- 643 Giese, J., Seward, D., Stuart, F.M., Wüthrich, E., Gnos, E., Kurz, D., Eggenberger, U. and  
644 Schreurs, G. (2010) Electrodynamic disaggregation: Does it affect apatite fission-track  
645 and (U-Th)/He Analyses? *Geostand. Geoanal. Res.* **34**, 39-48.
- 646 Glass, B.P., Liu, S. and Leavens, P.B. (2002) Reidite: An impact-produced high-pressure  
647 polymorph of zircon found in marine sediments. *Am. Mineral.* **87**, 562-565.
- 648 Goodenough, K.M. and Krabbendam, M. (2011) A geological excursion guide to the  
649 North-west Highlands of Scotland. NMSE Publishing, Edinburgh, UK. pp.228.
- 650 Grimes, C.B., John, B.E., Cheadle, M.J., Mazdab, F.K., Wooden, J.L., Swapp, S. and Schwartz,  
651 J.J. (2009) On the occurrence, trace element geochemistry, and crystallization history of  
652 zircon from *in situ* ocean lithosphere. *Contrib. Mineral. Petrol.* **158**, 757-783.
- 653 Hanchar, J.M. and van Westrenen, W. (2007) Rare earth element behavior in zircon-melt  
654 systems. *Elements* **3**, 37-42.
- 655 Harley, S.L. and Kelly, N.M. (2007) Zircon - tiny but timely. *Elements* **3**, 13-18.
- 656 Harley, S.L., Kelly, N.M. and Möller, A. (2007) Zircon behaviour and the thermal histories  
657 of mountain chains. *Elements* **3**, 25-30.
- 658 Harrison, T.M. (2009) The Hadean crust: Evidence from >4 Ga zircons. *Ann. Rev. Earth*  
659 *Planet. Sci.* **37**, 479-505.
- 660 Harrison, T.M. and Schmitt, A.K. (2007) High sensitivity mapping of Ti distributions in  
661 Hadean zircons. *Earth Planet. Sci. Lett.* **261**, 9-19.

- 662 Hawkesworth, C.J. and Kemp, A.I.S. (2006) Using hafnium and oxygen isotopes in zircons  
663 to unravel the record of crustal evolution. *Chem. Geol.* **226**, 144-162.
- 664 Hazen, R.M. and Finger, L.W. (1979) Crystal structure and compressibility of zircon at  
665 high pressure. *Am. Mineral.* **64**, 196-201.
- 666 Hellman, O.C., Vandenbroucke, J.A., Rüsing, J., Isheim, D. and Seidman, D.N. (2000)  
667 Analysis of three-dimensional atom-probe data by the proximity histogram. *Microsc.*  
668 *Micronanal.* **6**, 437-444.
- 669 Hinton, R. and Upton, B. (1991) The chemistry of zircon: Variations within and between  
670 large crystals from syenite and alkali basalt xenoliths. *Geochim. Cosmochim. Acta* **55**,  
671 3287-3302.
- 672 Horie, K., Hidaka, H. and Gauthier-Lafaye, F. (2006) Elemental distribution in zircon:  
673 Alteration and radiation-damage effects. *Phys. Chem. Earth.* **31**, 587-592.
- 674 Hoskin, P.W.O. (2000) Patterns of chaos: Fractal statistics and the oscillatory chemistry  
675 of zircon. *Geochim. Cosmochim. Acta* **64**, 1905-1923.
- 676 Hoskin, P.W.O. (2005) Trace-element composition of hydrothermal zircon and the  
677 alteration of Hadean zircon from the Jack Hills, Australia. *Geochim. Cosmochim. Acta* **69**,  
678 637-648.
- 679 Hoskin, P.W.O. and Black, L.P. (2000) Metamorphic zircon formation by solid-state  
680 recrystallization of protolith igneous zircon. *J. Metamorph. Geol.* **18**, 423-439.

- 681 Hoskin, P.W.O., Kinny, P.D., Wyborn, D. and Chappell, B.W. (2000) Identifying accessory  
682 mineral saturation during differentiation in granitoid magmas: an integrated approach.  
683 *J. Petrol.* **41**, 1365 -1396.
- 684 Hoskin, P.W.O. and Schaltegger, U. (2003) The composition of zircon and igneous and  
685 metamorphic petrogenesis. *Rev. Mineral. Geochem.* **53**, 27-62.
- 686 Humayun, M., Nemchin, A., Zanda, B., Hewins, R.H., Grange, M., Kennedy, A., Lorand, J.P.,  
687 Gopel, C., Fieni, C., Pont, S. and Deldicque, D. (2013) Origin and age of the earliest  
688 Martian crust from meteorite NWA 7533. *Nature* **503**, 513-516.
- 689 Iizuka, T., Yamaguchi, T., Hibiya, Y. and Amelin, Y. (2015) Meteorite zircon constraints on  
690 the bulk Lu–Hf isotope composition and early differentiation of the Earth. *Proc. Nat.*  
691 *Acad. Sci. U.S.A.* **112**, 5331-5336.
- 692 Johnson, T., Fischer, S., White, R., Brown, M. and Rollinson, H. (2012) Archaean  
693 intracrustal differentiation from partial melting of metagabbro—field and geochemical  
694 evidence from the central region of the Lewisian complex, NW Scotland. *J. Petrol.* **53**,  
695 2115-2138.
- 696 Kelly, T.F. and Larson, D.J. (2012) Atom probe tomography 2012. *Ann. Rev. Mater. Res.*  
697 **42**, 1-31.
- 698 Kingham, D.R. (1982) The post-ionization of field evaporated ions: A theoretical  
699 explanation of multiple charge states. *Surf. Sci.* **116**, 273-301.
- 700 Larson, D.J., Gault, B., Geiser, B.P., De Geuser, F. and Vurpillot, F. (2013a) Atom probe  
701 tomography spatial reconstruction: Status and directions. *Curr. Opin. Solid State Mater.*  
702 *Sci.* **17**, 236-247.

- 703 Larson, D.J., Prosa, T.J., Ulfig, R.M., Geiser, B.P. and Kelly, T.F. (2013b) Local Electrode  
704 Atom Probe: A User's Guide. Springer-Verlag New York. pp. 318.
- 705 Lee, H.B., Prinz, F.B. and Cai, W. (2013) Atomistic simulations of grain boundary  
706 segregation in nanocrystalline yttria-stabilized zirconia and gadolinia-doped ceria solid  
707 oxide electrolytes. *Acta Mater.* **61**, 3872-3887.
- 708 Leroux, H., Reimold, W.U., Koeberl, C., Hornemann, U. and Doukhan, J.C. (1999)  
709 Experimental shock deformation in zircon: a transmission electron microscopic study.  
710 *Earth Planet. Sci. Lett.* **169**, 291-301.
- 711 Maas, R., Kinny, P.D., Williams, I.S., Froude, D.O. and Compston, W. (1992) The Earth's  
712 oldest known crust: A geochronological and geochemical study of 3900-4200 Ma old  
713 detrital zircons from Mt. Narryer and Jack Hills, Western Australia. *Geochim. Cosmochim.*  
714 *Acta* **56**, 1281-1300.
- 715 Marsh, J.H. and Stockli, D.F. (2015) Zircon U-Pb and trace element zoning characteristics  
716 in an anatectic granulite domain: Insights from LASS-ICP-MS depth profiling. *Lithos* **239**,  
717 170-185.
- 718 Meis, C. and Gale, J.D. (1998) Computational study of tetravalent uranium and plutonium  
719 lattice diffusion in zircon. *Mater. Sci. Eng.* **B57**, 52-61.
- 720 Moser, D.E., Cupelli, C.L., Barker, I.R., Flowers, R.M., Bowman, J.R., Wooden, J. and Hart,  
721 J.R. (2011) New zircon shock phenomena and their use for dating and reconstruction of  
722 large impact structures revealed by electron nanobeam (EBSD, CL, EDS) and isotopic U-  
723 Pb and (U-Th)/He analysis of the Vredefort Dome. *Can. J. Earth Sci.* **48**, 117-139.



- 724 Moser, D.E., Davis, W.J., Reddy, S.M., Flemming, R.L. and Hart, R.J. (2009) Zircon U-Pb  
725 strain chronometry reveals deep impact-triggered flow. *Earth Planet. Sci. Lett.* **277**, 73-  
726 79.
- 727 Nasdala, L., Hanchar, J.M., Rhede, D., Kennedy, A.K. and Váczi, T. (2010) Retention of  
728 uranium in complexly altered zircon: An example from Bancroft, Ontario. *Chem. Geol.*  
729 **269**, 290-300.
- 730 Nemchin, A., Timms, N., Pidgeon, R., Geisler, T., Reddy, S. and Meyer, C. (2009) Timing of  
731 crystallization of the lunar magma ocean constrained by the oldest zircon. *Nat. Geosci.* **2**,  
732 133-136.
- 733 Nemchin, A.A., Grange, M.L. and Pidgeon, R.T. (2010) Distribution of rare earth elements  
734 in lunar zircon. *Am. Mineral.* **95**, 273-283.
- 735 Palenik, C.S., Nasdala, L. and Ewing, R.C. (2003) Radiation damage in zircon. *Am. Mineral.*  
736 **88**, 770-781.
- 737 Park, B., Weber, W.J. and Corrales, L.R. (2001) Molecular-dynamics simulation study of  
738 threshold displacements and defect formation in zircon. *Phys. Rev. B: Condens. Matter* **64**,  
739 174108.
- 740 Parman, S.W. (2015) Time-lapse zirconography: Imaging punctuated continental  
741 evolution. *Geochemical Perspectives Letters* **1**, 43-52.
- 742 Parnell, J., Mark, D., Fallick, A.E., Boyce, A. and Thackrey, S. (2011) The age of the  
743 Mesoproterozoic Stoer Group sedimentary and impact deposits, NW Scotland. *J. Geol.*  
744 *Soc.* **168**, 349-358.

- 745 Payne, J.L., McInerney, D.J., Barovich, K.M., Kirkland, C.L., Pearson, N.J. and Hand, M.  
746 (2016) Strengths and limitations of zircon Lu-Hf and O isotopes in modelling crustal  
747 growth. *Lithos* **248-251**, 175-192.
- 748 Peterman, E.M., Reddy, S.M., Saxey, D.W., Snoeyenbos, D.R., Rickard, W.D.A., Fougereuse,  
749 D. and Kylander-Clark, A.R.C. (2016) Nanogeochronology of a discordant zircon  
750 measured by atom probe microscopy of Pb-enriched dislocation loops. *Sci. Adv.* **2**,  
751 e1601318.
- 752 Piazzolo, S., Austrheim, H. and Whitehouse, M. (2012) Brittle-ductile microfabrics in  
753 naturally deformed zircon: Deformation mechanisms and consequences for U-Pb dating.  
754 *Am. Mineral.* **97**, 1544-1563.
- 755 Piazzolo, S., La Fontaine, A., Trimby, P., Harley, S., Yang, L., Armstrong, R. and Cairney, J.M.  
756 (2016) Deformation-induced trace element redistribution in zircon revealed using atom  
757 probe tomography. *Nat. Comms.* **7**, 10490.
- 758 Pidgeon, R.T. (2014) Zircon radiation damage ages. *Chem. Geol.* **367**, 13-22.
- 759 Portavoce, A. and Tréglia, G. (2014) Theoretical investigation of Cottrell atmosphere in  
760 silicon. *Acta Mater.* **65**, 1-9.
- 761 Rainbird, R.H., Hamilton, M.A. and Young, G.M. (2001) Detrital zircon geochronology and  
762 provenance of the Torridonian, NW Scotland. *J. Geol. Soc.* **158**, 15-27.
- 763 Reddy, S.M., Johnson, T.E., Fischer, S., Rickard, W.D.A. and Taylor, R.J.M. (2015)  
764 Precambrian reidite discovered in shocked zircon from the Stac Fada impactite,  
765 Scotland. *Geology* **43**, 899-902.

- 766 Reddy, S.M., Timms, N.E., Hamilton, P.J. and Smyth, H.R. (2009) Deformation-related  
767 microstructures in magmatic zircon and implications for diffusion. *Contrib. Mineral.*  
768 *Petrol.* **157**, 231-244.
- 769 Reddy, S.M., Timms, N.E., Pantleon, W. and Trimby, P. (2007) Quantitative  
770 characterization of plastic deformation of zircon and geological implications. *Contrib.*  
771 *Mineral. Petrol.* **153**, 625-645.
- 772 Reddy, S.M., Timms, N.E., Trimby, P., Kinny, P.D., Buchan, C. and Blake, K. (2006) Crystal-  
773 plastic deformation of zircon: A defect in the assumption of chemical robustness.  
774 *Geology* **34**, 257-260.
- 775 Simms, M.J. (2015) The Stac Fada impact ejecta deposit and the Lairg Gravity Low:  
776 evidence for a buried Precambrian impact crater in Scotland? *Proc. Geol. Assoc.* **126**,  
777 742-761.
- 778 Speer, J.A. (1980) Zircon, in: Ribbe, P.H. (Ed.), *Orthosilicates*. Mineralogical Society of  
779 America, Washington D.C., pp. 67-112.
- 780 Sun, L., Marrocchelli, D. and Yildiz, B. (2015) Edge dislocation slows down oxide ion  
781 diffusion in doped CeO<sub>2</sub> by segregation of charged defects. *Nat. Comms.* **6**, 6294.
- 782 Sutton, A. and Balluffi, R. (2006) *Interfaces in Crystalline Materials*. OUP Oxford, UK. pp.  
783 852.
- 784 Thompson, K., Flaitz, P.L., Ronsheim, P., Larson, D.J. and Kelly, T.F. (2007a) Imaging of  
785 arsenic Cottrell atmospheres around silicon defects by three-dimensional atom probe  
786 tomography. *Science* **317**, 1370-1374.

- 787 Thompson, K., Lawrence, D., Larson, D.J., Olson, J.D., Kelly, T.F. and Gorman, B. (2007b) In  
788 situ site-specific specimen preparation for atom probe tomography. *Ultramicroscopy*  
789 **107**, 131-139.
- 790 Timms, N.E., Kinny, P.D. and Reddy, S.M. (2006) Enhanced diffusion of Uranium and  
791 Thorium linked to crystal plasticity in zircon. *Geochem. Trans.* **7**:10.
- 792 Timms, N.E., Kinny, P.D., Reddy, S.M., Evans, K., Clark, C. and Healy, D. (2011)  
793 Relationship among titanium, rare earth elements, U-Pb ages and deformation  
794 microstructures in zircon: Implications for Ti-in-zircon thermometry. *Chem. Geol.* **280**,  
795 33-46.
- 796 Timms, N.E. and Reddy, S.M. (2009) Response of cathodoluminescence to crystal-plastic  
797 deformation in zircon. *Chem. Geol.* **261**, 11-23.
- 798 Timms, N.E., Reddy, S.M., Fitz Gerald, J.D., Green, L. and Muhling, J.R. (2012a) Inclusion-  
799 localised crystal-plasticity, dynamic porosity, and fast-diffusion pathway generation in  
800 zircon. *J. Struct. Geol.* **35**, 78-89.
- 801 Timms, N.E., Reddy, S.M., Healy, D., Nemchin, A.A., Grange, M.L., Pidgeon, R.T. and Hart, R.  
802 (2012b) Resolution of impact-related microstructures in lunar zircon: A shock-  
803 deformation mechanism map. *Meteorit. Planet. Sci.* **47**, 120-141.
- 804 Ushikubo, T., Kita, N.T., Cavosie, A.J., Wilde, S.A., Rudnick, R.L. and Valley, J.W. (2008)  
805 Lithium in Jack Hills zircons: Evidence for extensive weathering of Earth's earliest crust.  
806 *Earth Planet. Sci. Lett.* **272**, 666-676.

807 Valley, J.W., Cavosie, A.J., Ushikubo, T., Reinhard, D.A., Lawrence, D.F., Larson, D.J., Clifton,  
808 P.H., Kelly, T.F., Wilde, S.A. and Moser, D.E. (2014) Hadean age for a post-magma-ocean  
809 zircon confirmed by atom-probe tomography. *Nat. Geosci.* **7**, 219-223.

810 Valley, J.W., Reinhard, D.A., Cavosie, A.J., Ushikubo, T., Lawrence, D.F., Larson, D.J., Kelly,  
811 T.F., Snoeyenbos, D. and A, S. (2015) Nano- and Micro-geochronology in Hadean and  
812 Archean Zircons by Atom-Probe Tomography and SIMS: New Tools for Old Minerals. *Am.*  
813 *Mineral.* **100**, 1355-1377.

814 Vavra, G. (1990) On the kinematics of zircon growth and its petrogenetic significance: a  
815 cathodoluminescence study. *Contrib. Mineral. Petrol.* **106**, 90-99.

816 Watanabe, T. (1985) Structural effects on grain boundary segregation, hardening and  
817 fracture. *J. Phy. C.* **46**, 555-566.

818 Watson, E.B. and Harrison, T.M. (2005) Zircon thermometer reveals minimum melting  
819 conditions on earliest Earth. *Science* **308**, 841-844.

820 Wiedenbeck, M., Hanchar, J.M., Peck, W.H., Sylvester, P., Valley, J., Whitehouse, M., Kronz,  
821 A., Morishita, Y., Nasdala, L., Fiebig, J., Franchi, I., Girard, J.P., Greenwood, R.C., Hinton, R.,  
822 Kita, N., Mason, P.R.D., Norman, M., Ogasawara, M., Piccoli, P.M., Rhede, D., Satoh, H.,  
823 Schulz-Dobrick, B., Skår, O., Spicuzza, M.J., Terada, K., Tindle, A., Togashi, S., Vennemann,  
824 T., Xie, Q. and Zheng, Y.F. (2004) Further characterisation of the 91500 zircon crystal.  
825 *Geostand. Geoanal. Res.* **28**, 9-39.

826 Wilde, S.A., Valley, J.W., Peck, W.H. and Graham, C.M. (2001) Evidence from detrital  
827 zircons for the existence of continental crust and oceans on the Earth 4.4 Gyr ago. *Nature*  
828 **409**, 175-178.

829 Wittmann, A., Kenkmann, T., Schmitt, R.T. and Stoffler, D. (2006) Shock-metamorphosed  
830 zircon in terrestrial impact craters. *Meteorit. Planet. Sci.* **41**, 433-454.

831 Yoshiya, M. and Oyama, T. (2011) Impurity and vacancy segregation at symmetric tilt  
832 grain boundaries in Y<sub>2</sub>O<sub>3</sub>-doped ZrO<sub>2</sub>. *J. Mater. Sci.* **46**, 4176-4190.

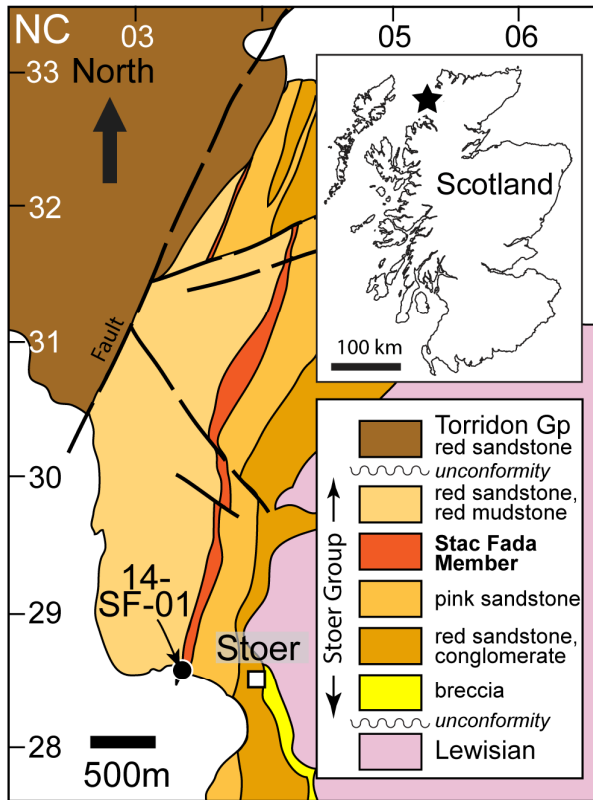
833

834

835

ACCEPTED MANUSCRIPT

Reddy et al: Figure 1



836

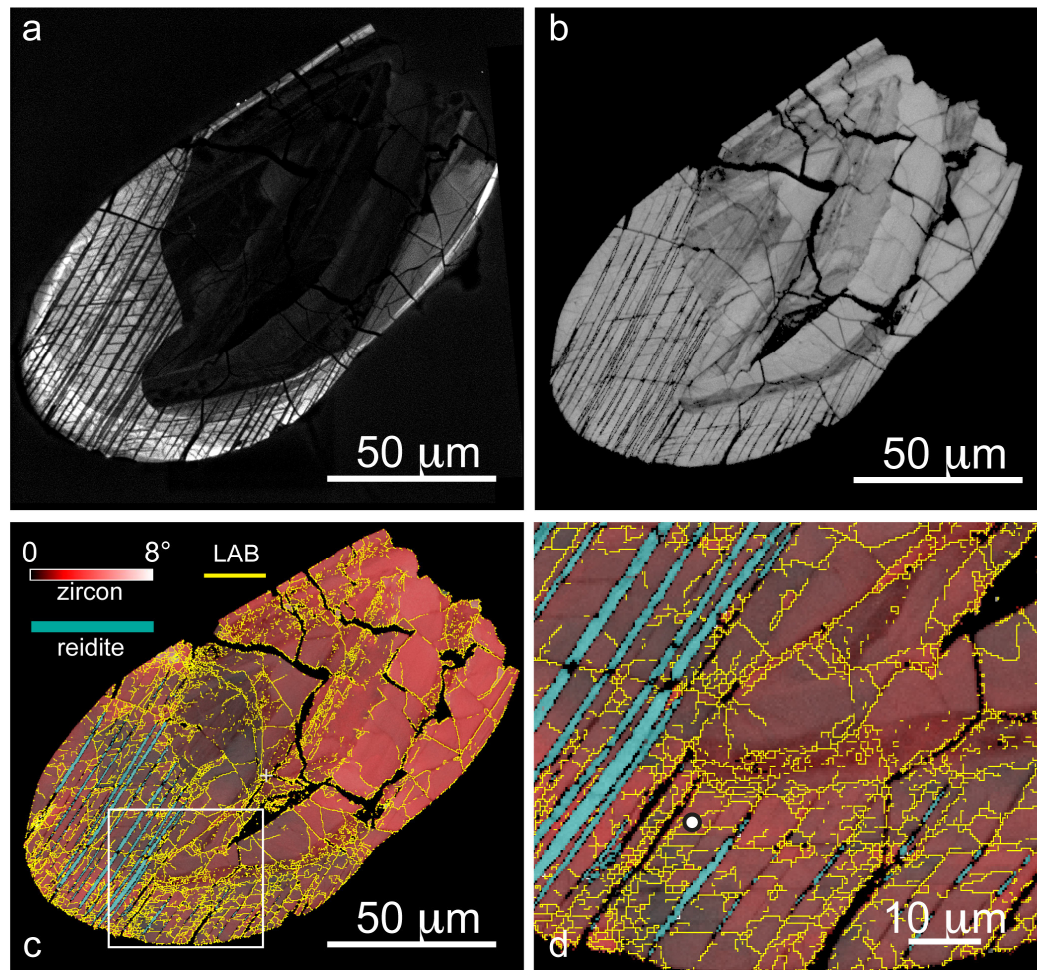
837

838

839

840

Reddy et al - Fig. 2



841

842

843

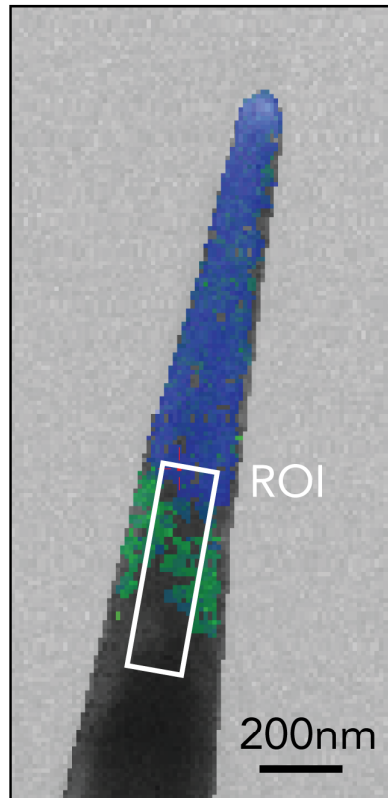
844

845

846



Reddy et al Fig. 3



MANUSCRIPT

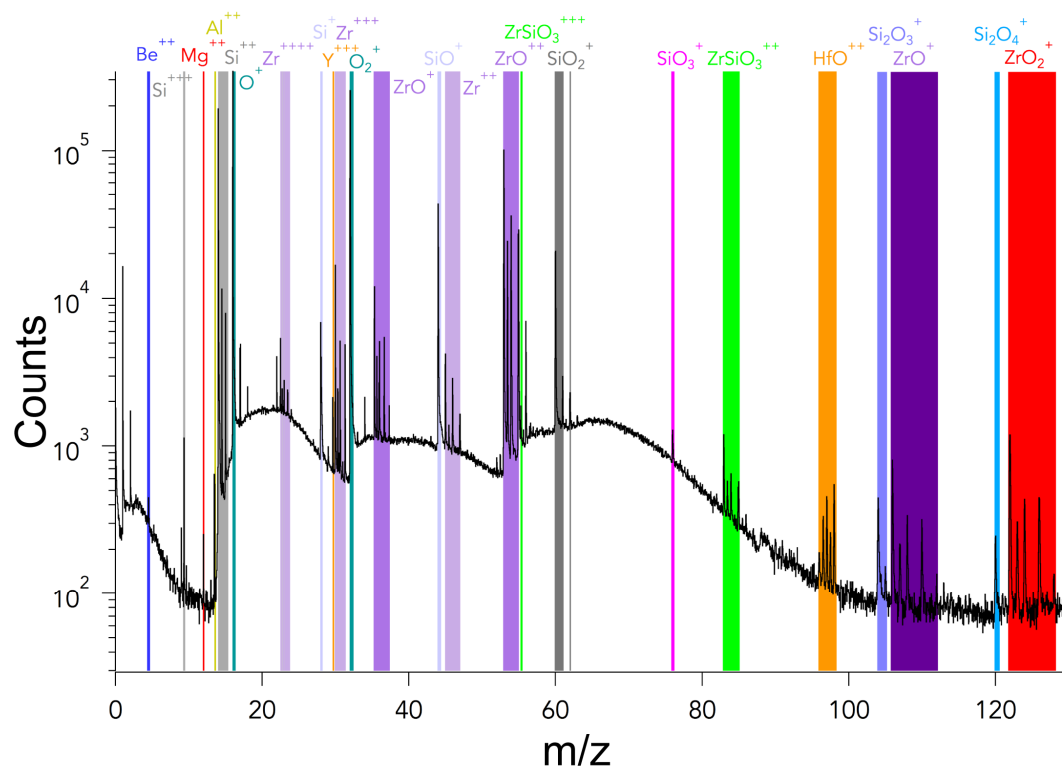
847

848

849

850

Reddy et al - Fig04



851

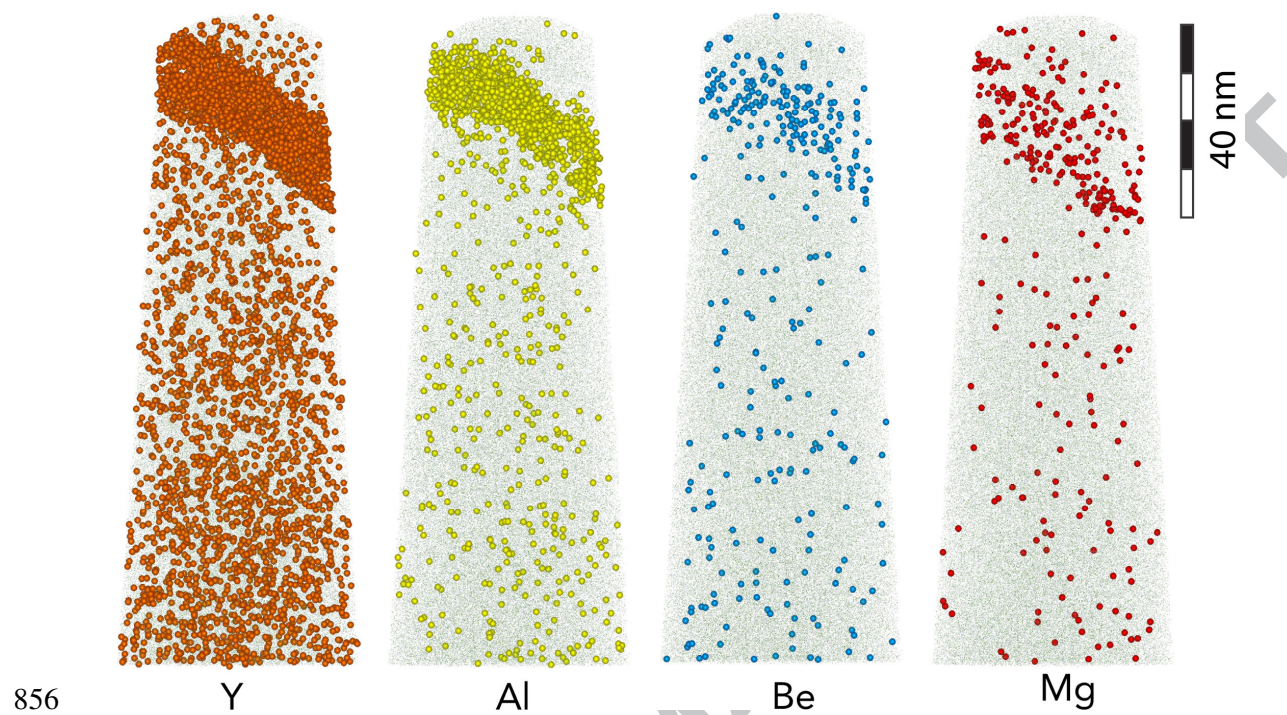
852

853

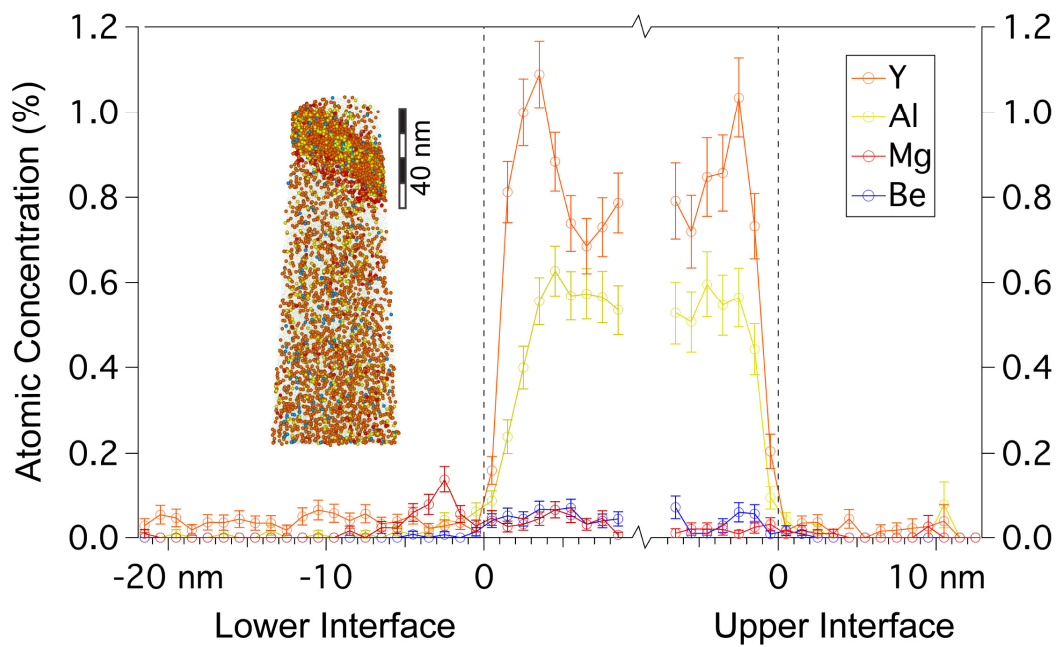
854

855

Reddy et al. Fig 5



Reddy et al Fig. 6



860

861

862

863

ACCEPTED MANUSCRIPT

|         | Matrix        |                   | Low-angle boundary |                   |
|---------|---------------|-------------------|--------------------|-------------------|
| Element | Concentration | +/- (1 $\sigma$ ) | Concentration      | +/- (1 $\sigma$ ) |
| Zr      | 17.71%        | 0.03%             | 16.03%             | 0.09%             |
| Si      | 15.61%        | 0.03%             | 15.88%             | 0.09%             |
| O       | 66.51%        | 0.07%             | 66.54%             | 0.23%             |
| Hf      | 0.141%        | 0.002%            | 0.106%             | 0.007%            |
| Y       | 0.013%        | 0.001%            | 0.735%             | 0.019%            |
| Al      | 0.0041%       | 0.0004%           | 0.543%             | 0.016%            |
| Be      | 0.0044%       | 0.0004%           | 0.055%             | 0.005%            |
| Mg      | -             | -                 | 0.029%             | 0.004%            |

864

865

866

867 Table 1

868